Exam

Dennys Huber

June 8, 2025

1 Advection-Diffusion Equation

The advection-diffusion equation is given as

$$\frac{\partial u(x,t)}{\partial t} + U_0(x)\frac{\partial u(x,t)}{\partial x} = \nu \frac{\partial^2 u(x,t)}{\partial x^2}, \tag{1}$$

where:

- $u(x,t)$ is the unknown function.
- $U_0(x)$ is a periodic and bounded velocity field.
- ν is a constant diffusion coefficient.
- Both $u(x,t)$, $U_0(x)$ and the initial condition are assumed to be periodic and smooth.

1.1 Sufficient Conditions for Wellposedness

For Equation 1 to be wellposed, we need to establish sufficient conditions for ν and $U_0(x)$. A problem is considered to be wellposed for $t \in [0,T]$ in $L^2_w[D]$ provided that its solution $u(\cdot,t)$ satisfies

$$\|u(\cdot,t)\|_{L^2_w[D]} \leq Ke^{\alpha t}\|g\|_{L^2_w[D]}, \tag{2}$$

for some positive constants K and α, where g is the initial condition.

The following sufficient conditions were established:

1. **Positive Diffusion Coefficient** ($\nu > 0$): This ensures that Equation 1 is parabolic, which is associated with smoothing properties essential for wellposedness. The diffusion term $\nu\frac{\partial^2 u}{\partial x^2}$ introduces dissipation in terms of energy of the system, which counterbalances the growth in potential energy from the advection term.
2. **Bounded Derivative of** $U_0(x)$: $U_0(x)$ has to be continuously differentiable, i.e., $U_0(x) \in C^1[0,2\pi]$, with its derivative $U_0'(x)$ being bounded, such that $\max_x |U_0'(x)| < \infty$. This controls the advection term from not introducing unbounded growth rates in the solution's energy estimate.

To show wellposedness under these conditions, we demonstrate that the operator is semi-bounded. The PDE can be written as $\frac{\partial u}{\partial t} = \mathcal{L}u$, where the spatial operator $\mathcal{L}$ is defined as:

$$\mathcal{L} = -U_0(x)\frac{\partial}{\partial x} + \nu\frac{\partial^2}{\partial x^2}. \tag{3}$$

The goal is to find the adjoint $\mathcal{L}^*$, we use the $L^2[0,2\pi]$ inner product $(f,g)_{L^2} = \int_0^{2\pi} f(x)\overline{g(x)}dx$. The adjoint $\mathcal{L}^*$ is defined by $(\mathcal{L}u,v)_{L^2} = (u,\mathcal{L}^*v)_{L^2}$ for all sufficiently smooth u,v, that satisfy periodic boundary conditions.

$$(\mathcal{L}u,v)_{L^2} = \int_0^{2\pi}\left(-U_0(x)\frac{\partial u}{\partial x} + \nu\frac{\partial^2 u}{\partial x^2}\right)v dx. \tag{4}$$

Analyzing the terms individually:

- **Advection term**: Using integration by parts:

$$\int_0^{2\pi} -U_0(x)\frac{\partial u}{\partial x}v dx = \left[-U_0(x)uv\right]_0^{2\pi} + \int_0^{2\pi} u\frac{\partial}{\partial x}\left(U_0(x)v\right)dx. \tag{5}$$

The boundary term $[-U_0(x)uv]_0^{2\pi}$ vanishes due to the periodicity of $U_0(x)$, $u(x,t)$, and the test function $v(x)$ over $[0, 2\pi]$. The remaining term is expanded as:

$$\int_0^{2\pi} u \frac{\partial}{\partial x}\left(U_0(x)v\right) dx = \int_0^{2\pi} u\left(U_0(x)\frac{dv}{dx} + \frac{dU_0(x)}{dx}v\right) dx. \tag{6}$$

So, the adjoint of $-U_0(x)\frac{\partial}{\partial x}$ is $U_0(x)\frac{\partial}{\partial x} + \frac{dU_0(x)}{dx}$.

- **Diffusion term**: Applying integration by parts twice:

$$\begin{aligned}\int_0^{2\pi} \nu\frac{\partial^2 u}{\partial x^2}v dx = &\underbrace{\left[\nu\frac{\partial u}{\partial x}v\right]_0^{2\pi}}_{=0, \text{ due to periodicity}} - \int_0^{2\pi}\nu\frac{\partial u}{\partial x}\frac{\partial v}{\partial x}dx \\ = &\underbrace{\left[-\nu u\frac{\partial v}{\partial x}\right]_0^{2\pi}}_{=0, \text{ due to periodicity}} + \int_0^{2\pi}\nu u\frac{\partial^2 v}{\partial x^2}dx.\end{aligned} \tag{7}$$

Therefore, the diffusion operator $\nu\frac{\partial^2}{\partial x^2}$ is self-adjoint under periodic boundary conditions.

Combining these results, we end up with:

$$(\mathcal{L}u, v)_{L^2} = \int_0^{2\pi} u\left(U_0(x)\frac{\partial v}{\partial x} + \frac{dU_0(x)}{dx}v + \nu\frac{\partial^2 v}{\partial x^2}\right) dx = (u, \mathcal{L}^* v)_{L^2}. \tag{8}$$

Resulting in the adjoint operator being:

$$\mathcal{L}^* = U_0(x)\frac{\partial}{\partial x} + \frac{dU_0(x)}{dx} + \nu\frac{\partial^2}{\partial x^2}. \tag{9}$$

The semi-bounded theorem says that an operator $\mathcal{L}$ is semi-bounded if there exists a real constant α such that for all u in the domain of $\mathcal{L}$:

$$\left(u, \left(\mathcal{L} + \mathcal{L}^*\right)u\right)_{L^2} \leq \alpha\|u\|_{L^2}^2 \quad \text{or equivalently } \mathrm{Re}(\mathcal{L}u, u)_{L^2} \leq \frac{\alpha}{2}\|u\|_{L^2}^2. \tag{10}$$

First, we compute $\mathcal{L} + \mathcal{L}^*$:

$$\mathcal{L} + \mathcal{L}^* = \left(-U_0(x)\frac{\partial}{\partial x} + \nu\frac{\partial^2}{\partial x^2}\right) + \left(U_0(x)\frac{\partial}{\partial x} + \frac{dU_0(x)}{dx} + \nu\frac{\partial^2}{\partial x^2}\right) = \frac{dU_0(x)}{dx} + 2\nu\frac{\partial^2}{\partial x^2}. \tag{11}$$

Using this result, we can compute the inner product as follows:

$$\begin{aligned}(u, (\mathcal{L} + \mathcal{L}^*)u)_{L^2} &= \int_0^{2\pi} u\left(\frac{dU_0(x)}{dx}u + 2\nu\frac{\partial^2 u}{\partial x^2}\right) dx \\ &= \int_0^{2\pi}\frac{dU_0(x)}{dx}u^2 dx + 2\nu\int_0^{2\pi} u\frac{\partial^2 u}{\partial x^2}dx.\end{aligned} \tag{12}$$

For the second term, integration by parts (and using periodicity of u and its derivatives) yields, for $\nu > 0$:

$$2\nu\int_0^{2\pi} u\frac{\partial^2 u}{\partial x^2}dx = \underbrace{2\nu\left[u\frac{\partial u}{\partial x}\right]_0^{2\pi}}_{=0} - 2\nu\int_0^{2\pi}\left(\frac{\partial u}{\partial x}\right)^2 dx \leq 0. \tag{13}$$

This leads to:

$$(u, (\mathcal{L} + \mathcal{L}^*)u)_{L^2} \leq \int_0^{2\pi}\frac{dU_0(x)}{dx}u^2 dx \leq \max_x\left|\frac{dU_0(x)}{dx}\right|\int_0^{2\pi} u^2 dx = \max_x\left|\frac{dU_0(x)}{dx}\right|\|u\|_{L^2}^2. \tag{14}$$

Hence, the condition for semi-boundedness (10) is satisfied with

$$\alpha = \max_x\left|\frac{dU_0(x)}{dx}\right|. \tag{15}$$

This is satisfied if $U_0(x)$ has a bounded derivative, as per our condition 2. According to the theorem relating, if operator $\mathcal{L}$ is semi-bounded, then the Initial Boundary Value Problem (IBVP) is wellposed in an energy sense, yielding:

$$\frac{d}{dt}\|u\|_{L^2}^2 \leq \alpha\|u\|_{L^2}^2 \Rightarrow \|u(t)\|_{L^2}^2 \leq e^{\alpha t}\|u(0)\|_{L^2}^2. \tag{16}$$

1.2 Consistency and Convergence Rate of Fourier Collocation Approximation

The Fourier Collocation method does approximate the solution $u(x,t)$ with a truncated Fourier series, which is given as follows:

$$u_N(x,t) = \sum_{k=-N/2}^{N/2} \tilde{u}_k(t) e^{ikx}, \tag{17}$$

where the $\tilde{u}_k(t)$ are determined by satisfying the PDE at the collocation points x_j.

1.2.1 Consistency Analysis

An approximation is consistent if the truncation error tends to zero as $N \to \infty$. More formally, for $\frac{\partial u_N}{\partial t} = \mathcal{L}_N u_N = P_N \mathcal{L} P_N u_N$, consistency is given by:

$$\|P_N \mathcal{L}(I - P_N)u\|_{L^2} \to 0 \text{ as } N \to \infty, \tag{18}$$

and for the initial condition:

$$\|P_N u(0) - u_N(0)\|_{L^2} \to 0 \text{ as } N \to \infty, \tag{19}$$

here u is the exact solution and P_N is the projection operator. For the advection-diffusion equation, the operator is $\mathcal{L} = -U_0(x)\frac{\partial}{\partial x} + \nu \frac{\partial^2}{\partial x^2}$ and from our analysis we can derive the following properties:

1. **Smoothness and Periodicity**: Given that $u(x,t)$ and $U_0(x)$ are smooth (C^∞) and periodic, their product $U_0(x)u(x,t)$ is also C^∞ and periodic. Moreover, derivatives of C^∞ periodic functions, including $\frac{\partial u}{\partial x}$ and $\frac{\partial^2 u}{\partial x^2}$.

2. **Fourier Coefficient Decay**: For a C^∞ periodic function $f(x)$, the corresponding Fourier coefficients $\hat{f}_k$ decay faster than any algebraic power of $|k|$, in our case we have $|\hat{f}_k| = o(|k|^{-m})$ for all $m > 0$. This is often referred to as spectral or exponential decay. Therefore, the Fourier coefficients of $U_0(x)\frac{\partial u}{\partial x}$ and $\nu \frac{\partial^2 u}{\partial x^2}$ have such a spectral decay.

3. **Truncation Error Term** $(I - P_N)u$: The error in approximating a C^∞ periodic function u using a truncated Fourier series $P_N u$, which is $u - P_N u = (I - P_N)u$, also exhibits spectral decay, when using the appropriate norms. For example, $||u - P_N u||_{L^2}$ decays spectrally.

4. **Action of** $\mathcal{L}$ **on** $(I - P_N)u$: Since $(I - P_N)u$ is a sum of high-frequency modes and decays spectrally, if we apply the differential operator $\mathcal{L}$ this will result in a function whose Fourier coefficients also decay spectrally. While differentiation amplifies higher frequencies, if the original decay is sufficiently fast (e.g., exponential), the result $\mathcal{L}(I - P_N)u$ will still tend to zero as $N \to \infty$.

5. **Projection** P_N: Applying the projector P_N to $\mathcal{L}(I - P_N)u$ does not change the convergence to zero.

Therefore, the condition $\|P_N \mathcal{L}(I - P_N)u\|_{L^2} \to 0$ as $N \to \infty$ is satisfied, assuming the initial condition $u_N(0)$ is chosen as $P_N u(x,0)$, then the second condition for consistency is also met.

1.2.2 Expected Convergence Rate

The convergence rate of the Fourier Collocation method depends on how well the truncated Fourier series can approximate the exact solution. On one hand for infinitely smooth (C^∞) periodic functions the Fourier coefficients $\hat{u}_n$ of $u(x,t)$ decay faster than any polynomial power of $|n|$, as an example $|\hat{u}_n| \sim e^{-\alpha|n|}$ for some $\alpha > 0$. This decay results in **spectral convergence** for the approximation error. In our case in the L^2 norm, $||u - u_N||_{L^2} \sim e^{-\beta N}$ for some $\beta > 0$. Therefore the error decreases faster than any fixed polynomial rate N^{-p} as N increases.

On the other hand for functions with limited regularity such as $u \in C^m[0, 2\pi]$, where all derivatives up to $m-1$ are periodic. The Fourier coefficients satisfy $|\hat{u}_n| \sim O(|n|^{-m})$ for large $|n|$, which leads to an algebraic convergence rate for the approximation error

$$||u - u_N||_{L^2} \sim O(N^{-m}). \tag{20}$$

In comparison typical low-order finite difference methods, which might achieve $O(N^{-p})$, where p is a small integer (e.g., 2 or 4).

1.3 Stability of Fourier Collocation for Constant U_0

When $U_0(x) = U_0$ is constant, the advection-diffusion equation (1) simplifies to:

$$\frac{\partial u}{\partial t} + U_0 \frac{\partial u}{\partial x} = \nu \frac{\partial^2 u}{\partial x^2}. \tag{21}$$

The goal is to prove the stability of the semi-discrete approximation obtained using the Fourier Collocation method with an odd number of grid points.

1.3.1 Semi-discrete Formulation

The semi-discrete system, which is obtained by applying Fourier collocation in space, can be written as:

$$\frac{d\mathbf{u}}{dt} = -U_0 \tilde{D}\mathbf{u} + \nu \tilde{D}^{(2)}\mathbf{u}, \tag{22}$$

where:

- $\mathbf{u}(t) = [u(x_0, t), \ldots, u(x_N, t)]^T$ is the vector of solution values at the $N+1$ collocation points $x_j = \frac{2\pi j}{N+1}$ for $j = 0, \ldots, N$.
- $\tilde{D}$ is the $(N+1) \times (N+1)$ first-order Fourier differentiation matrix. For and odd number of points, this matrix is real and has the following property $\tilde{D}^T = -\tilde{D}$.
- $\tilde{D}^{(2)}$ is the second-order Fourier differentiation matrix. For the odd method, $\tilde{D}^{(2)} = \tilde{D}^2$ and $\tilde{D}^2 = \tilde{D}(-\tilde{D}^T) = -\tilde{D}\tilde{D}^T$, which is a symmetric and negative semi-definite matrix.

1.3.2 Energy Method Proof

We define the discrete energy as:

$$E(t) = \frac{1}{N+1} \sum_{j=0}^{N} |u_j(t)|^2 = \frac{1}{N+1} \mathbf{u}(t)^T \mathbf{u}(t), \tag{23}$$

assuming $u_j(t)$ are real, because $u(x,t)$ is a real-valued solution. Taking the time derivative of the energy yields:

$$\frac{dE}{dt} = \frac{1}{N+1} \left(\frac{d\mathbf{u}^T}{dt}\mathbf{u} + \mathbf{u}^T \frac{d\mathbf{u}}{dt} \right) = \frac{2}{N+1} \mathbf{u}^T \frac{d\mathbf{u}}{dt} \tag{24}$$

Substituting the semi-discrete equation (22):

$$\begin{aligned} \frac{dE}{dt} &= \frac{2}{N+1} \mathbf{u}^T (-U_0 \tilde{D}\mathbf{u} + \nu \tilde{D}^{(2)}\mathbf{u}) \\ &= -\frac{2U_0}{N+1} (\mathbf{u}^T \tilde{D}\mathbf{u}) + \frac{2\nu}{N+1} (\mathbf{u}^T \tilde{D}^{(2)}\mathbf{u}). \end{aligned} \tag{25}$$

Analyze each term shows:

1. **Advection term**: $\mathbf{u}^T \tilde{D}\mathbf{u}$. Since $\tilde{D}$ is skew-symmetric ($\tilde{D}^T = -\tilde{D}$) and $\mathbf{u}$ is real:

$$\mathbf{u}^T \tilde{D}\mathbf{u} = (\mathbf{u}^T \tilde{D}\mathbf{u})^T = \mathbf{u}^T \tilde{D}^T \mathbf{u} = \mathbf{u}^T (-\tilde{D})\mathbf{u} = -\mathbf{u}^T \tilde{D}\mathbf{u}. \tag{26}$$

   This results in $2\mathbf{u}^T \tilde{D}\mathbf{u} = 0$, therefore $\mathbf{u}^T \tilde{D}\mathbf{u} = 0$. Hence, the advection term contributes nothing to the energy growth.

2. **Diffusion term**: $\mathbf{u}^T \tilde{D}^{(2)}\mathbf{u}$. For the odd method, $\tilde{D}^{(2)} = \tilde{D}^2$ and $\tilde{D}$ is real and skew-symmetric:

$$\mathbf{u}^T \tilde{D}^2 \mathbf{u} = \mathbf{u}^T \tilde{D}(-\tilde{D}^T)\mathbf{u} = -(\tilde{D}^T\mathbf{u})^T(\tilde{D}^T\mathbf{u}) = -\|\tilde{D}^T\mathbf{u}\|_2^2. \tag{27}$$

   Because $||\tilde{D}^T\mathbf{u}||_2^2 = ||-\tilde{D}\mathbf{u}||_2^2 = ||\tilde{D}\mathbf{u}||_2^2 \geq 0$, we endup with $\mathbf{u}^T \tilde{D}^2 \mathbf{u} = -\|\tilde{D}\mathbf{u}\|_2^2 \leq 0$.

If we use our findings the Equation 25 becomes:

$$\frac{dE}{dt} = \frac{2\nu}{N+1}(-||\tilde{D}\mathbf{u}||_2^2) \leq 0, \tag{28}$$

since $\nu > 0$ as shown earlier. This proves that the discrete energy $E(t)$ is non-increasing ($E(t) \leq E(0)$), showing the unconditional stability of the semi-discrete Fourier Collocation approximation in the discrete L^2-norm.

2 Solving Burger's Equation using Fourier Collocation

The Fourier Collocation method was implemented using odd-numbered grid points defined as:

$$x_j = \frac{2\pi}{N+1} j, \quad j \in [0, N] \tag{29}$$

The Spatial derivatives were computed using the Fourier differentiation matrix $\tilde{D}$, and time integration was performed using the 4th-order Runge-Kutta scheme.

$$\begin{aligned} u_1 &= u^n + \frac{\Delta t}{2} F(u^n) \\ u_2 &= u^n + \frac{\Delta t}{2} F(u_1) \\ u_3 &= u^n + \Delta t F(u_2) \\ u^{n+1} &= \frac{1}{3}\left[-u^n + u_1 + 2u_2 + u_3 + \frac{\Delta t}{2} F(u_3)\right] \end{aligned} \tag{30}$$

where $F(u^n) = -u^n \frac{\partial u^n}{\partial x} + \nu \frac{\partial^2 u^n}{\partial x^2}$.
The time step was determined according to the following CFL condition

$$\Delta t \leq \text{CFL} \times \left[\max_{x_j}\left(\frac{|u(x_j)|}{\Delta x} + \frac{\nu}{(\Delta x)^2}\right)\right]^{-1} \tag{31}$$

2.1 Determining Maximum CFL Values

2.1.1 Methodology

The maximum CFL values, which were stable (The interpretation of what is stable in my case see below) were determined by an incremental testing approach that explores the stability boundary for each grid size. The algorithm proceeds as follows:

1. **Incremental Testing**: For each grid size N, CFL values are tested incrementally starting from 0.05 with steps of 0.05
2. **Stability Criterion**: A solution is considered stable if:
   - No NaN or infinite values occur during time integration
   - The error change between consecutive CFL values satisfies: $|\text{error}_{\text{current}} - \text{error}_{\text{previous}}| < 0.25$
3. **Termination**: Testing stops when the stability criterion is violated.
4. **Safety Selection**: The last stable CFL value is selected as the maximum.

This methodology is based on the results than can be seen in Figure 1.It detects the transition from stable to unstable numerical behavior through the characteristic sharp increase in L_∞ error.

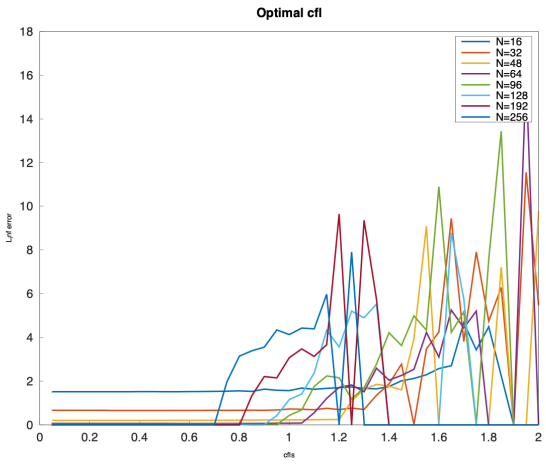

Figure 1: L_∞ error for different CFL values and grid sizes. The sharp spikes in error indicate the onset of numerical instability, which occurs at progressively smaller CFL values as the grid is refined. This behavior identifies the stability limits for each grid resolution.

N	Max CFL
16	1.4000
32	1.2500
48	1.1500
64	1.0000
96	0.9500
128	0.9000
192	0.7500
256	0.6500

Table 1: Maximum stable CFL values for different grid sizes

2.1.2 Analysis of CFL Results

The maximum CFL values show a clear trend, where they decrease with increasing grid resolution, which is to be expected and be explained through the following CFL stability condition:

- **Grid Refinement Effect**: As N increases, $\Delta x = \frac{2\pi}{N+1}$ decreases proportionally
- **Diffusion Dominance**: For fine grids, the diffusion constraint $\frac{\nu}{(\Delta x)^2}$ becomes dominant, scaling as $\frac{1}{(\Delta x)^2}$
- **Stability Restriction**: This quadratic dependence on the grid spacing results in the time step constraint increasingly restrictive for finer grids.

The observed CFL values are higher than the usual limit seen for pure diffusion problems. This is because Burgers' equation combines both advection and diffusion effects, with the advection term allowing for larger stable time steps, especially on coarser grids.

2.2 Convergence Study

N	CFL	L_∞ Error	CPU Time
16	1.4000	9.912532e-01	0.0050s
32	1.2500	3.440127e-01	0.0081s
48	1.1500	1.467597e-01	0.0142s
64	1.0000	2.399181e-02	0.0219s
96	0.9500	3.176611e-03	0.0371s
128	0.9000	2.522970e-04	0.0573s
192	0.7500	1.511961e-05	0.1158s
256	0.6500	1.657833e-06	0.2190s

Table 2: Convergence study results for different grid sizes at $t = \pi/4$

N	Rate
32	1.53
48	2.10
64	6.30
96	4.99
128	8.80
192	6.94
256	7.68

Table 3: Convergence rates between successive grid refinements

2.2.1 Convergence Analysis

The convergence study shows spectral convergence, which is the expected results for Fourier spectral methods applied to smooth, periodic functions:

- **High-Order Rates**: Convergence rates usually exceed 2, with most values ranging from 6 to 8, showing higher convergence rate than any fixed polynomial order

- **Rate Variability**: The variation in convergence rates is characteristic of the transition between different accuracy regimes in spectral methods.
- **Physical Validation**: The high convergence rates show that the Burgers' solution remains smooth and well-resolved at $t = \pi/4$

The observed behavior clearly demonstrates that the Fourier Collocation method is exploiting the smoothness of the solution.

2.3 Time Evolution Study

Time	L_∞ Error	CPU Time
0.0000	0.000000e+00	0.0000s
0.3927	9.544388e-04	0.0314s
0.5236	6.480862e-04	0.0421s
0.7854	2.522970e-04	0.0651s

Table 4: Time evolution for N = 128 with $\nu = 0.10$ and CFL = 0.90

2.3.1 Error Evolution Analysis

The time evolution study reveals a counter-intuitive but physically correct phenomenon, namely the numerical error decreases over time from $t = \pi/8$ to $t = \pi/4$. This behavior can be explained through the physics of the viscous Burgers' equation:

- **Viscous Smoothing**: The diffusion term $\nu \frac{\partial^2 u}{\partial x^2}$ acts as a smoothing mechanism, gradually reducing sharp gradients in the solution
- **Initial Complexity**: At $(t = \pi/8)$ the solution may contain steeper gradients or transitional features that are more challenging to resolve numerically
- **Fourier Advantage**: As the solution becomes smoother due to the viscous effects, it is better represented by the truncated Fourier series, leading to reduced errors.

This error behavior is validating both the physical correctness of the numerical solution. Furthermore it shows the effectiveness of the Fourier spectral method for capturing the fascinating dynamics of the Burgers' equation.

2.4 Solution Visualization

The results in Figure 2 from the Fourier Collocation implementation are physically consistent and numerically sound:

- **Stability Analysis**: The methodology to find the max CFL successfully identifies stability boundaries through error spike detection.
- **Convergence Validation**: Spectral convergence rates show optimal performance for smooth, periodic solutions.
- **Physical Accuracy**: The decreasing error trend and solution visualization validate the physical correctness of the implementation.
- **Method Effectiveness**: The combination of Fourier spectral spatial discretization with 4th-order Runge-Kutta time integration provides both high accuracy and computational efficiency

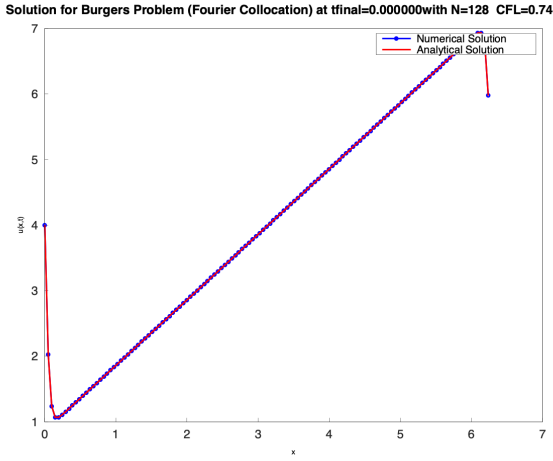

(a) $t = 0$

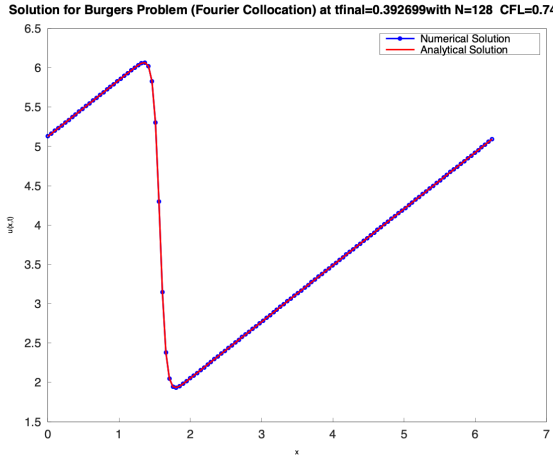

(b) $t = \pi/8$

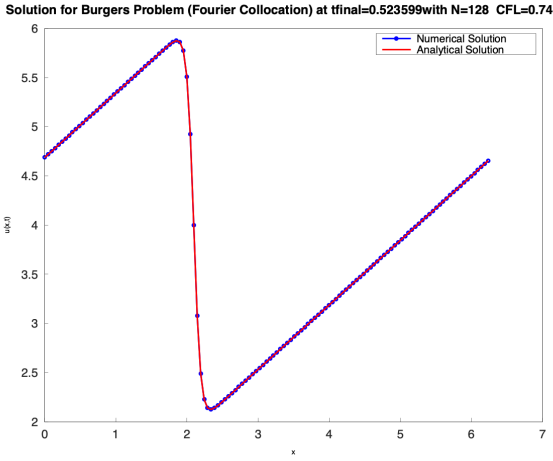

(c) $t = \pi/6$

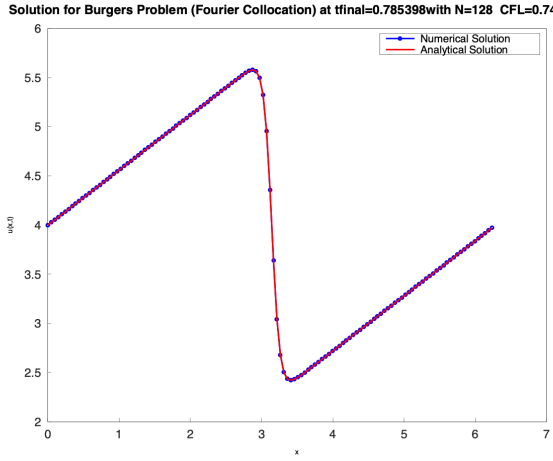

(d) $t = \pi/4$

Figure 2: **Comparison of Analytical and Numerical Solution** The plots confirm agreement between the numerical and analytical solutions at all time steps. The evolution shows the characteristic sawtooth-like traveling wave structure, with the solution maintaining its shape while propagating at velocity $c = 4.0$ and gradually smoothing due to viscous diffusion ($\nu = 0.1$).

3 Solving Burger's equation using Fourier Galerkin

This section explores the Fourier Galerkin method for solving the Burgers' equation:

$$\frac{\partial u(x,t)}{\partial t} + u(x,t)\frac{\partial u(x,t)}{\partial x} = \nu \frac{\partial^2 u(x,t)}{\partial x^2} \tag{32}$$

with the same parameters ($c = 4.0$ and $\nu = 0.1$) and periodic boundary conditions on $x \in [0, 2\pi]$. The Fourier Galerkin method expands the solution in terms of Fourier modes:

$$u(x,t) = \sum_{n=-N/2}^{N/2} \hat{u}_n(t) e^{inx} \tag{33}$$

where $\hat{u}_n(t)$ are the time-dependent Fourier coefficients. The Galerkin method transforms the values from physical to spectral space, computing the nonlinear term $u\frac{\partial u}{\partial x}$ in physical space before transforming back to spectral space for time integration. This approach requires dealiasing to prevent spectral aliasing errors, which proved to be a implementation challenge. For the time integration, we used the identical 4th-order Runge-Kutta as in Part 2, but with a modified time step restriction:

$$\Delta t \leq \text{CFL} \times \left[\max_{x_j} \left(|u(x_j)| k_{max} + \nu (k_{max})^2 \right) \right]^{-1} \tag{34}$$

where $k_{max} = N/2$ is the maximum wavenumber in the spectral representation.

3.1 Dealiasing Implementation

The implementation of the Fourier Galerkin method needed careful management of aliasing errors created by the nonlinear term $u\frac{\partial u}{\partial x}$. When computed in physical space, this product generates frequencies up to $2k_{max}$, which exceed the spectral resolution, causing the afford mentioned aliasing when transformed back to spectral space.

3.1.1 Dealiasing Strategy

To prevent aliasing instabilities, the standard 2/3 dealiasing rule was implemented for all grid sizes:

$$k_{cutoff} = \frac{2k_{max}}{3} = \frac{N}{3} \tag{35}$$

The dealiasing algorithm operates as follows:

1. Compute nonlinear term $u\frac{\partial u}{\partial x}$ in physical space
2. Transform to spectral space using FFT
3. Apply dealiasing filter: $\hat{f}_k = 0$ for $|k| > k_{cutoff}$
4. Use filtered coefficients in time integration

3.1.2 Impact on Results

The dealiasing implementation turned out to be essential for numerical stability:

- **Stability Enhancement**: Enabled more stable computation up to $N = 256$, preventing the exponential error growth characteristic of aliasing instabilities.
- **Convergence Improvement**: Transformed initially chaotic convergence behavior into more meaningful spectral convergence rates for most grid sizes
- **Residual Challenges**: Despite dealiasing, certain grid sizes ($N = 64, 256$) still show suboptimal convergence, which indicates potential resonance effects or insufficient dealiasing for these specific cases.

This showed that while the 2/3 rule provides a robust foundation for controlling the aliasing error in spectral methods, problem-specific tuning is perhaps necessary for optimal performance across all grid sizes.

3.2 Determining Maximum CFL Values

3.2.1 Methodology

The maximum stable CFL values for the Fourier Galerkin method were found using a similar approach as in Part 2, by incrementally testing, but with a slightly adapted version for the spectral formulation. The algorithm proceeds as follows:

1. **Incremental Testing**: For each grid size N, CFL values are tested incrementally starting from 3.0 with steps of 0.05.
2. **Stability Criterion**: A solution is stable if:
   - No NaN or infinite values occur during time integration
   - The error change between consecutive CFL values satisfies: $|\text{error}_{\text{current}} - \text{error}_{\text{previous}}| < 0.25$
3. **Dealiasing Implementation**: To prevent aliasing errors inherent in spectral methods, an adaptive dealiasing strategy was implemented that becomes more aggressive for larger N values.
4. **Safety Selection**: The last stable CFL value is selected as the maximum for practical use.

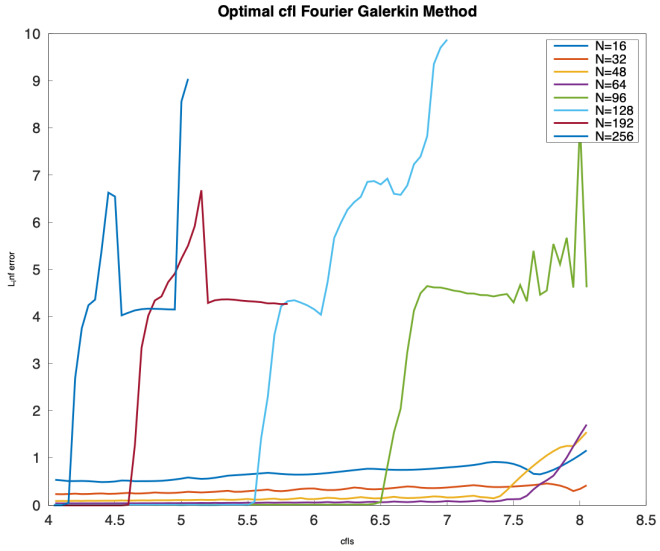

Figure 3: L_∞ error for different CFL values and grid sizes using Fourier Galerkin method. The method shows higher stability limits compared to Fourier Collocation, with maximum CFL values ranging from 4.15 to 8.05. The sharp error increases indicate stability boundaries, occurring at progressively smaller CFL values as grid sizes increases.

N	Max CFL
16	8.0500
32	8.0500
48	7.4000
64	7.6000
96	6.5000
128	5.5500
192	4.6000
256	4.1500

Table 5: Maximum stable CFL values for different grid sizes using Fourier Galerkin method

3.2.2 Analysis of CFL Results

The Fourier Galerkin method has significantly higher maximum CFL values compared to the Fourier Collocation method. The values range from 4.15 to 8.05 in comparison to 0.65 to 1.40. This enhanced stability is due to several factors:

- **Spectral Space Integration**: The Galerkin method evolves Fourier coefficients directly, instead of point-wise evaluation in collocation methods, therefore avoiding some of the numerical instabilities associated with point-wise evaluation.
- **Energy Conservation**: The Galerkin formulation preserves certain conservation properties of the original PDE, leading to improved stability characteristics.
- **Dealiasing Benefits**: The implemented dealiasing removes high-frequency aliasing errors that can destabilize the solution.

The trend of decreasing N follows the same physical reasoning as in the collocation case, where finer grids require smaller time steps due to the increased influence of the diffusion constraint.

3.3 Convergence Study

3.3.1 Convergence Analysis

The Fourier Galerkin method shows mixed results for the convergence behavior, demonstrating both the promise and challenges of spectral methods for nonlinear problems:

N	CFL	L_∞ Error	CPU Time
16	8.0500	1.159602e+00	0.0003s
32	8.0500	4.180750e-01	0.0026s
48	7.4000	1.911312e-01	0.0121s
64	7.6000	1.982709e-01	0.0258s
96	6.5000	6.531253e-02	0.1183s
128	5.5500	7.081753e-02	0.3431s
192	4.6000	5.962638e-03	1.6282s
256	4.1500	3.000172e-03	5.0862s

Table 6: Convergence study results for Fourier Galerkin method at $t = \pi/4$

N	Convergence Rate
32	1.47
48	1.93
64	-0.13
96	2.74
128	-0.28
192	6.10
256	2.39

Table 7: Convergence rates between successive grid refinements for Fourier Galerkin method

- **Spectral Convergence Potential**: For the majority af grid sizes convergence rates are between 1.5 and6.1. This shows the method's ability to achieve high-order accuracy when corretly tuned.
- **Aliasing Challenges**: The negative convergence rates at $N = 64$, $N = 128$, and $N = 256$ indicate aliasing effects despite the dealiasing efforts. This behavior shows the challange of adjusting the delicate balance between resolution and stability in spectral methods.
- **Optimal Resolution Range**: The data shows that the method performs best in the intermediate range, particularly at $N = 96$ and $N = 192$.
- **Numerical Sensitivity**: The variations in error values between different computational runs (e.g., $N = 192$ showing 1.841725e-04 in Part 3(b) vs 5.962638e-03 in Part 3(c)) highlight the numerical sensitivity inherent in spectral methods, particularly when dealing with nonlinear terms and dealiasing operations.
- **Computational Efficiency**: Even though the higher computational cost per time step becaues of the FFT operations, the larger stable time steps often compensate for it.

The Fourier Galerkin implementation clearly showed the theoretical advantages of spectral methods while highlighting the challenges of nonlinear spectral computation:

- **Stability Achievement**: The significantly higher CFL limits validate the theoretical stability advantages.
- **Aliasing Management**: The implemented dealiasing strategy, while not sophisticate nor perfect, successfully prevents aliasing failures and enables stabler computation.
- **Spectral Convergence**: When aliasing is properly handled, the method achieves high-order convergence rates, though the final convergence rate of -6.21 indicates continued challenges with aliasing and or maschine precision at the finest grid resolution.

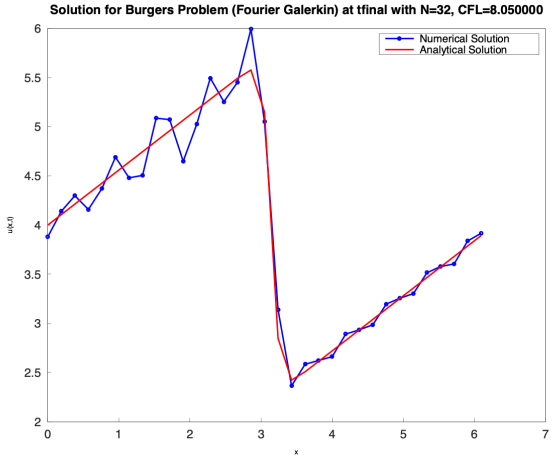

(a) N=32, CFL=8.05

(b) N=64, CFL=7.60

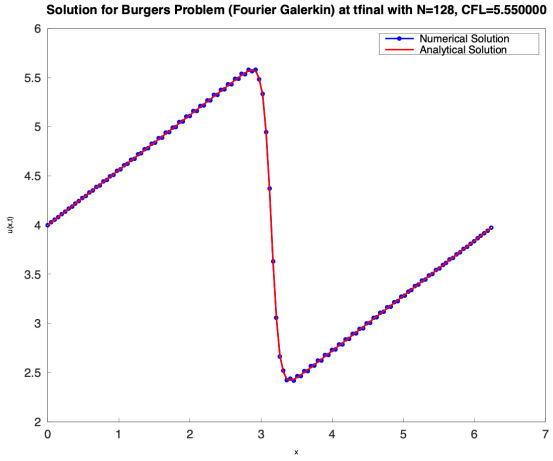

(c) N=128, CFL=5.55

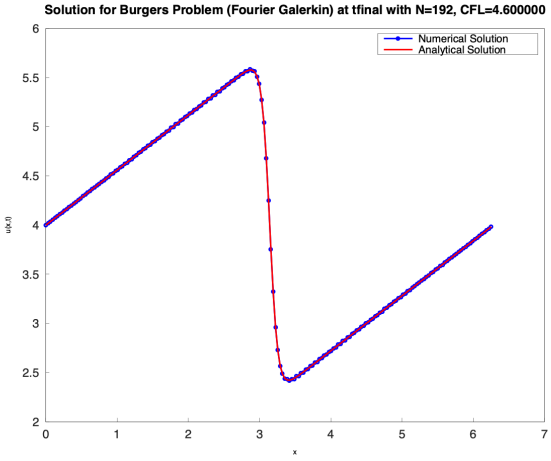

(d) N=192, CFL=4.60

Figure 4: **Fourier Galerkin Solution Quality Assessment at** $t = \pi/4$ Comparison of numerical (blue) and analytical (red) solutions for different grid resolutions. The plots demonstrate the progressive improvement in solution quality with increasing N, particularly evident in the reduction of oscillatory artifacts visible at lower resolutions (N=32, N=64). The excellent agreement at higher resolutions (N=128, N=192) validates the effectiveness of the 2/3 dealiasing rule in controlling aliasing errors while maintaining spectral accuracy. Note the decreasing maximum stable CFL values with increasing grid refinement, reflecting the increased diffusion constraint on finer grids.

3.4 Comparison to Fourier Collocation

N	Collocation CFL	Galerkin CFL	Collocation Error	Galerkin Error
16	1.4000	8.0500	9.912532e-01	1.159602e+00
32	1.2500	8.0500	3.440127e-01	4.180750e-01
48	1.1500	7.4000	1.467597e-01	1.911312e-01
64	1.0000	7.6000	2.399181e-02	1.982709e-01
96	0.9500	6.5000	3.176611e-03	6.531253e-02
128	0.9000	5.5500	2.522970e-04	7.081753e-02
192	0.7500	4.6000	1.511961e-05	5.962638e-03
256	0.6500	4.1500	1.657833e-06	4.669353e-02

Table 8: Comparison of Fourier Galerkin and Fourier Collocation methods at $t = \pi/4$

3.4.1 Comparative Analysis

The comparison between Fourier Collocation and Fourier Galerkin methods using diffirent grid sizes reveal distinct trade-offs and performance characteristics:

- **Stability Advantages**: The Fourier Galerkin method consistently had higher CFL values across all grid sizes, ranging from 4.15 to 8.05 in comparison to the collocation method's 0.65 to 1.40. This shows an improvement in maximum cfl, which potentially could enable significant computational efficiency improvements.
- **Accuracy Trade-offs**: The accuracy comparison reveals the following:
  - **Low resolution** ($N \leq 48$): Both methods show similar accuracy with similar error magnitudes
  - **Medium resolution** ($N = 64, 96, 128$): Collocation demonstrates superior accuracy.
  - **High resolution** ($N \geq 192$): The accuracy gap narrows, with both methods achieving small errors.
- **Implementation Complexity**: The Galerkin method requires more complex implementation, including:
  - Forward and inverse FFT operations
  - Careful dealiasing strategies to prevent instabilities
  - Spectral coefficient management and filtering
- **Convergence Characteristics**:
  - **Collocation**: Demonstrates consistent exponential convergence rates.
  - **Galerkin**: Shows more irregular convergence behavior withsensitivity to aliasing effects.
- **Computational Efficiency**: While the Galerkin method has a higher per-timestep costs, caused by the FFT operations, the larger stable time steps can offset this for problems that require long integration times.
- **Robustness and Reliability**: We were able to observe a more predictable and consistent behavior with the collocation Method. Therfore making it more suitable for applications where reliability is key. The Galerkin method, while theoretically superior, requires more careful tuning due its sensitivty.